2.6% cm −2 Single-Pass CO 2 -to-CO Conversion Using Ni Single Atoms Supported on Ultra-Thin Carbon Nanosheets in a Flow Electrolyzer

Yang Zhang, Kun Qi, Ji Li, Bonito A Karamoko, Luc Lajaunie, Franck Godiard, Erwan Oliviero, Xiaoqiang Cui, Ying Wang, Yupeng Zhang, et al.

2.6 % cm^{-2} single-pass CO_2-to-CO conversion using Ni single-atoms supported on ultra-thin carbon nanosheets in a flow electrolyzer

Yang Zhang[1,2], Kun Qi[2], Ji Li[3], Bonito A. Karamoko[2], Luc Lajaunie[4,5], Franck Godiard[6], Erwan Oliviero[6], Xiaoqiang Cui[7], Ying Wang[7], Yupeng Zhang[1], Huali Wu[2], Wensen Wang[2], Damien Voiry[2]*

[1] Key Laboratory of Optoelectronic Devices and Systems of Ministry of Education and Guangdong Province, College of Optoelectronic Engineering, Shenzhen University, Shenzhen, 518000, China

[2] Institut Européen des Membranes, IEM, UMR 5635, Université Montpellier, ENSCM, CNRS, Montpellier, 34090, France

[3] College of Bioresources Chemical and Materials Engineering, Shaanxi University of Science and Technology, Xi'an, 710000, China

[4,5] Departamento de Ciencia de los Materiales e Ingeniería Metalúrgica y Química Inorgánica, Instituto Universitario de Investigación de Microscopía Electrónica y Materiales (IMEYMAT), Facultad de Ciencias, Universidad de Cádiz, Campus Río San Pedro S/N, Puerto Real, Cádiz, 11510, Spain

[6] MEA Platform, University of Montpellier, Montpellier, 34090, France.

[7] State Key Laboratory of Automotive Simulation and Control, Department of Materials Science, Key Laboratory of Automobile Materials of MOE, Jilin University, Changchun, 130000, China.

Keywords: CO_2 reduction reaction, single-atom catalysts, flow electrolyzers, three-phase interface, single pass conversions.

ABSTRACT

The CO_2 reduction reaction using a renewable energy source is a promising strategy for its utilization. Such a technology however requires the development of catalysts with optimized activity and selectivity that can be integrated into the device architectures. Flow electrolyzers have recently been proposed for facilitating the electrochemical CO_2 reduction reaction thanks to their unique ability to perform electroreduction at high reaction rates *via* the creation of three-phase interface. While some examples of flow electrolyzers for the conversion of CO_2 has recently been reported, the influence of the CO_2 and electrolyte streams on the overall catalytic mechanism is remained ambiguous. Here, we synthesized single-atom nickel on two-dimensional nitrogen-doped carbon nanosheets (SA Ni-NC) for the CO_2-to-CO conversion. Taking advantage of this model catalyst, we explored the correlation between the applied potential and the feeds in both

electrolyte and CO_2 on the one hand, and the performance metrics on the other hand. By regulating the feed stream's conditions, the SA Ni-NC achieves energy efficiencies as high as 85% at j_{CO} = 7.2 mA cm^{-2} and 56% at j_{CO} = 170 mA cm^{-2} whereas the single-pass CO_2-to-CO conversion efficiency (SPCC) reaches 2.6% cm^{-2}. We finally demonstrated the scalability of the flow electrolyzers by stacking three 1-cm^2 reactors and reached a record-high CO yield rate of 31.5 L min^{-1} m^{-2} with near-unity CO selectivity and an SPCC of 8.9% from three.

1. Introduction

The intensive consumption of fossil fuels along with excessive emission of carbon dioxide (CO_2) exacerbate global environmental problems, which severely limits the potential of sustainable growth.[1] The CO_2 capture and utilization technologies are being investigated to mitigate the release of CO_2 into the atmosphere.[2] Among the various strategies, the electrochemical CO_2 reduction reaction (CO_2RR) under ambient conditions, which can be coupled with renewable electricity sources, represents a promising approach to reuse the CO_2 emissions, while generating value-added fuels and chemicals.[3,4] In this context, a vast amount of efforts are currently being devoted to the development of novel electrocatalysts with optimum selectivity and activity towards the production of various C_1-C_3 molecules.[5,6] The discovery of single-atom catalysts has extended new directions for the rational design of heterogeneous catalysts

with well-defined structure and maximum exposure of the active sites.[7] Single-atom catalysts have been demonstrated with outstanding electrochemical CO_2RR selectivity and high current densities thanks to the peculiar coordination environment of the single metal atom and the local electronic structures that differs from those of the nanoparticle counterparts.[8-10] Specifically, nitrogen-doped carbon with the inclusions of metal single atoms (M-N-C) has been investigated for several key electrochemical reactions including the hydrogen evolution reaction (HER), the oxygen reduction reaction (ORR) and also the CO_2RR.[11-13]

The search for highly active CO_2RR catalysts is typically carried out using traditional "H-cell" reactors. The performance is however severely limited by the relatively low CO_2 dissolvability in the liquid electrolyte. H-cell designs also face mass transport limitation and high proton transfer resistance, thus leading to the current densities typically lower than 100 mA cm^{-2} which precluding its industrial applications.[12] To unlock these bottlenecks, novel device architectures have recently been reported using solid-state electrolytes or flow reactors. Specifically, mass transport limitations can efficiently be overcame thanks to the continuously feed in the electrolyte and CO_2 and current densities up to 1 A cm^{-2} have recently been reported.[14-16] In flow electrolyzers, the reduction of CO_2 occurs at the three-phase interface, which is formed by CO_2 (gas), the electrolyte (liquid) and the catalyst (solid) respectively. This strategy ensures an efficient supply of CO_2 meanwhile electrons and protons for the successive electron-proton coupled transfers associated with the reaction pathway.[17] Two main strategies

are usually adopted in order to enhance the CO_2RR activity and selectivity using flow electrolyzers: *i)* improve the intrinsic activity of the catalysts and *ii)* engineer the structure of the gas diffusion electrodes (GDE). For example, by changing the structure of catalysts, the porosity of the carbon support, or the hydrophilic/hydrophobic properties of the electrode, the CO_2 diffusion length can be greatly reduced and the mass transport will be significantly accelerated.[18-22]

In addition to the design of the catalyst and the manipulation of electrode those all focus on the optimizing of the solid phase for three-phase interface, the feed stream's conditions of both the electrolyte (liquid) and CO_2 (gas) are therefore expected to play a central role in the kinetics of the CO_2RR and the final CO_2-to-product conversion efficiency.[23] For example, by tuning the gas flow rates, the transport of CO_2 to the surface of the catalyst as well as its local concentration can be directly controlled to optimize the equilibrium between the adsorption of CO_2 and the desorption of the products on the active sites.[24-26] This is particularly crucial concerning the reaction processes at high conversion rates – *i.e.* at high current densities. For example, if we consider the conversion of CO_2 to carbon monoxide (CO), a current density of 100 mA cm^{-2} – considered to be a threshold value for any industrial application – involves a turnover of $\approx 6.2 \times 10^{17}$ cm^{-2} molecules of CO_2 and protons per second. To date, the understanding of the influence of electrolyte and CO_2 feeds on the overall CO_2RR performance – notably the energy efficiency of the reaction – in flow electrolyzers has remained elusive.

Herein, we investigate the behavior of single atom nickel supported on ultrathin nitrogen-doped carbon nanosheets (SA Ni-NC) in a flow electrolyzer for the electrocatalytic conversion of CO_2-to-CO. The SA Ni-NC demonstrates excellent CO_2RR stability together with a near-unity CO_2-to-CO selectivity; making it an ideal platform to investigate the feedstock parameters in a flow electrolyzer. By tuning the electrolyte or CO_2 flow rates, we explored the role of the CO_2 and electrolyte feeds on the electrochemical CO_2RR properties and the reaction rates at the three-phase interface. The optimum flow allowed achieving current densities as high as 170 mA cm^{-2} with an ultra-high energy efficiency ranging up to 85%. We finally demonstrate the scalability of our catalyst by connecting up to three flow electrolyzers in series to reach a single-pass CO_2-to-CO conversion of 8.9 % and a yield rate of $\approx$ 31.5 L min^{-1} m^{-2} while maintaining a near-unity CO_2-to-CO selectivity. Our work highlights the importance of the understanding of the flow dynamics in CO_2RR to optimize the energy efficiency, the single-pass conversion as well as the yield rate of the reaction, which are key parameters for the development of industrial-scale processes towards the conversion of CO_2-to-CO.

2. Results and discussion

2.1. Density functional theory calculations and catalyst selection

We first performed density functional theory (DFT) calculations to identify a model CO_2RR catalyst for the conversion of CO_2-to-CO with high efficiency and selectivity. **Figure 1a** shows the successive steps associated with the CO_2 electrochemical

reduction pathways on the optimized structures of atomic nickel coordinated by four pyrrolic nitrogen: NiN_4 supported on a carbon nanosheet. The reaction pathways for the CO_2 electroreduction to CO is known to proceed *via* two successive proton-coupled electron transfer (PCET) associated with the formation of *COOH and *CO intermediates.[27,28] The energy profile associated with the CO_2-to-CO conversion has been calculated for the NiN_4 and Ni (111) for comparison (**Figure 1b**). We first note that the barrier energy associated with CO_2-to-CO reaction on the NiN_4 is 0.1 eV smaller than that on Ni (111). The corresponding Gibbs free energy plot for the above-mentioned Ni-based catalysts suggests that the free energy change of Ni (111) for the formation of the *COOH intermediate is lower compared with that of NiN_4 at 0.09 eV and 1.56 eV respectively. The formation of *COOH on NiN_4 is endergonic and corresponds to the common rate-determining step for the CO_2RR on the single-atom sites. This first PCET process is followed by the formation of *CO for both catalysts. The *CO desorption from NiN_4 is then exothermic with a free energy change of 0.75 eV contrary to Ni (111), for which the desorption is endergonic with an associated free energy change of 1.65 eV. We examined the influence of the applied potential on the electrochemical CO_2RR performance for NiN_4 and Ni (111), respectively. As shown in **Figure 1c** and **1d**, the free energy change of the rate-determining step for NiN_4 decreases with the applied potential increasing, while it remains virtually constant in the case of Ni (111). The predictions therefore suggest that the increase of the overpotential does not yield to an improved catalytic activity towards the production of

CO for Ni (111). In addition, the DFT calculations of HER show that the first protonation step for Ni (111) is spontaneous, and the energy barrier for the formation of 1/2 H_2 is estimated to be 0.36 eV – much smaller than the *CO desorption energy barrier of 1.63 eV (**Figure S1**). Our results indicate that the NiN_4 sites supported on carbon are promising to deliver high CO_2-to-CO selectively thanks to an efficient desorption step, and a reduced barrier energy of rate-determining step at increasing overpotentials. Conversely the Ni (111) sites are likely to be poisoned due to the rate-determining step associated with the desorption of *CO. To further understand the nature of binding of CO on NiN_4 and Ni (111), the projected density of states (PDOS) was calculated in the presence and absence of CO, respectively. After the geometry optimization, we found that the 3d orbitals of the active sites on Ni (111) hybridize with the 5 σ and 2 π * orbitals of CO, presenting strong chemisorption of CO molecules on Ni (111) (**Figure 1e**). However, in the case of the NiN_4 sites, CO spontaneously desorbs and no obvious orbital hybridization of CO and activate sites was observed. The distance between the nickel atoms of NiN_4 and the carbon atoms of CO was estimated to be larger than 3 Å, suggesting weak Van der Waals' interactions and confirming facile desorption of the produced CO molecules. Our results thus predict again that the rapid desorption of CO on NiN_4 plays a key role in the selectivity of the CO_2RR towards the production of CO.

2.2. Catalyst characterization and electrode preparation

In the light of the DFT results, single-atom nickel with well-defined catalytically active sites on ultrathin supported on two-dimensional (2D) nitrogen-doped carbon nanosheets (SA Ni-NC) was prepared. The as-prepared catalyst exhibits a two-dimensional structure with a smooth surface as confirmed by scanning electron microscopy and atomic force microscopy characterizations (**Figure 2a**, **Figure S2**). To provide compelling evidence of the uniform distribution of the nickel atoms on the nitrogen-doped carbon nanosheets, we performed energy dispersive X-ray (EDX) mapping on the SA Ni-NC nanosheets. EDX analyses revealed that the Ni, C, and N elements are homogeneously distributed at the scale of the flake without noticeable metal aggregation or formation of the Ni nanoparticles (**Figure 2b-2e**). The nature of the Ni atoms in SA Ni-NC was further characterized by aberration-corrected high-angle annular dark-field scanning transmission electron microscopy (HAADF-STEM). Ni atoms are observed as brighter spots due to their larger atomic number compared with those of carbon and nitrogen. Ultra-small bright dots from the nickel single-atoms are found on SA Ni-NC confirming the uniform dispersion of the nickel with an average size of 0.15 ± 0.04 nm as confirmed by the HAADF-STEM and electron energy-loss spectroscopy (EELS) mapping (**Figure 2f**, **Figure S3**). To investigate the chemical composition and oxidation state of Ni, X-ray photoelectron spectroscopy (XPS) was performed on the SA Ni-NC (**Figure S4**). The Ni 2p spectrum of SA Ni-NC appears as doublets corresponding to Ni 2p3/2 (855.5 eV) and Ni 2p1/2 (873.5 eV) respectively. We observe a positive shift of the binding energy compared with that of bulk Ni –

expected at 852.4 eV and 869.6 eV for Ni 2p3/2 and Ni 2p1/2 respectively, which reveals a higher oxidation state for Ni as expected for the NiN_x sites of the single atoms.[9,29] The high-resolution N 1s XPS spectrum of SA Ni-NC exhibits four peaks located at 398.0, 400.5 and 401.2 eV, which are assigned to the pyridinic N, pyrrolic N and graphitic N, respectively.[8] Besides, the peak at a binding energy of 399.3 eV is attributed to the presence of N atoms coordinated by metal and points out the presence of Ni-N bonds in the case of SA Ni-NC. According to the XPS data, the atomic ratio of N to Ni was estimated to be 2.7, which can be ascribed to the presence of a trace amount of encapsulated Ni aggregates in the carbon layer. The atomic C : N ratio on the carbon flakes was estimated by XPS and EELS to be between 9.2% and 11.5% respectively (**Figure S5**). The oxidation state of the Ni atoms in SA Ni-NC was further determined from the position of the rising edge of the Ni K-edge X-ray absorption near edge structure (XANES). A positive peak offset is observed with respect to the position of the K-edge of the reference nickel foil; in qualitative agreement with the shift observed from the Ni 2p region in XPS (**Figure S6a**). The final evidence of the single-atomic nature of the SA Ni-NC was provided by the extended X-ray absorption fine structure (EXAFS) measurements. We obtained a good agreement between the Fourier transformed EXAFS spectrum of SA Ni-NC in k-space and the simulated spectrum of Ni–N_4, which indicates the presence of Ni-N_4 sites on SA Ni-NC (Inset **Figure 2g, Figure S6b and Table S1**). And the Fourier transform of the phase uncorrected EXAFS spectra of SA Ni-NC displayed a prominent peak at 1.42 Å (**Figure 2g**). Such a value

is shorter than the Ni-Ni interactions in Ni foil at 2.15 Å and attributed to the presence of Ni-N interactions, in perfect agreement with the presence of isolated nickel atoms on the nitrogen-doped carbon nanosheet for SA Ni-NC.

2.3. Investigations of the CO_2RR activity in an H-cell reactor

To gauge the electrochemical CO_2RR performance, the SA Ni-NC catalyst was first tested using a traditional H-cell equipped with a cation exchange membrane between the anode and cathode chambers. A CO_2-saturated solution consisting of 0.1 M KOH + 0.5 M K_2SO_4 was used as the electrolyte and the catalyst was immobilized on a mechanically polished glassy carbon electrode with a geometric loading of 0.044 mg cm^{-2} (See Experimental section for details). To observe the influence of the single-atom nature of the Ni sites on the CO_2RR properties, we first compared the performance of SA Ni-NC with that of Ni nanoparticles supported on reduced graphene oxide (Ni-NPC) under the same conditions. The gas and liquid products were analyzed using gas chromatography (GC) and nuclear magnetic resonance (NMR) respectively. Hydrogen (H_2) and CO were found to be the only products of the reaction for both SA Ni-NC and Ni-NPC catalysts. The linear scan voltammetry (LSV) curves demonstrate that Ni-NPC has a larger reduction current at a large range of applied potential compared with that of SA Ni-NC (**Figure 3a**), while most of the current works for hydrogen evolution. The onset potential of SA Ni-NC for CO_2RR to occur is about -0.25 V *vs.* the reversible hydrogen electrode (RHE), which compares favorably with the recently reported values in the literature.[9,16,30] Remarkably, the Faradaic efficiency of CO (FE_{CO}) for SA Ni-NC

is much larger than that for Ni-NPC and the FE_{CO} reaches the highest value of about 80% at an applied potential of -0.75 V *vs.* RHE (**Figure 3b**). At this applied potential, the partial current density of CO (j_{CO}) reaches -1.87 mA cm^{-2} and -0.77 mA cm^{-2} for the SA Ni-NC and Ni-NPC, respectively. We also observe that the reactions on Ni-NPC are dominated by the HER process – i.e. the production of H_2 – and the Ni nanoparticles are poorly selective towards CO_2RR (**Figure 3c**). The high selectivity of the NiN_4 sites compared with Ni nanoparticles is in line with our numerical predictions and attributed to the rapid desorption of *CO. To further assess the potential of SA Ni-NC as a CO_2RR catalyst, we evaluated the electrochemical stability of the catalyst over 48 h at an applied potential of -0.8 V *vs.* RHE (**Figure 3d**). The current was continuously measured while the gas products were injected into the gas chromatograph every 3 hours. The SA Ni-NC catalyst exhibits a stable cathodic current density and negligible drop of FE_{CO} as demonstrated by retentions of 92.5% and 95% respectively (Figure 3d). We also measured the electrochemical double-layer capacity (C_{dl}) and the electrochemical impedance spectroscopy (EIS) of the two catalysts (**Figure S7 and Table S2**). The results show that SA Ni-NC catalyst exhibits a better interfacial charge transfer and more electrochemical active sites for CO_2RR. All of the above results indicate that SA Ni-NC holds promises as a CO_2RR catalyst with excellent selectivity and stability towards the production of CO from CO_2.

2.4. Investigations of the CO_2RR activity in a flow electrolyzer

The performance of SA Ni-NC was further evaluated in a liquid-electrolyte flow electrolyzer using CO_2-saturated mixture of 0.1 M KOH+0.5 M K_2SO_4 solution as the electrolyte for both the cathode and the anode chambers. The catalyst was loaded on a GDE and the downstream products of the reaction were continuously analyzed using gas chromatography. The model 1 cm^2 flow reactor allows for the continuous diffusion of CO_2 to the catalyst layer thanks to the position of the supported catalyst directly at the gas/liquid interface (**Figure S8**). To scrutinize the relationship between the CO_2RR properties and the CO_2/electrolyte feedstocks, the flow rates for both the electrolyte and CO_2 were controllably tuned from 20 to 100 mL min^{-1} and 20 to 140 mL min^{-1}, respectively. The specific current density and Faradaic efficiency were measured at different potentials for each feed parameters, which allowed us to elucidate the behavior of SA Ni-NC in the flow electrolyzer. The electrochemical CO_2RR properties of the SA Ni-NC were first assessed at a fixed stream of 60 ml min^{-1} CO_2 with the variation of electrolyte flow rates (**Figure 4a**). The highest current reaches ≈ 170 mA cm^{-2} at -1.15 V *vs.* RHE for a 60 mL min^{-1} electrolyte flow rate while the FE_{CO} shows near-unity selectivity for all electrolyte flow rates – sharply improved compared with that measured in H-cell (**Figure 4b and** Figure 3b). It should be noted that, due to the experimental errors introduced by the GC analyzes, the measured CO selectivity could sometimes be slightly higher than 100%, especially when H_2 was suppressed to below 1%.[31] To further study the effects of the electrolyte flow rate on the CO_2RR performance from the viewpoint of three-phase interface, we analyzed both the

electrochemical impedance spectra (EIS) of the catalyst and the double-layer capacitance (C_{dl}) (**Figure 4c** and **4d**).[32] As shown in Figure 4d, the C_{dl} values get larger with the increase of the electrolyte flow rate and reaches a plateau for flow rates > 60 mL min^{-1}. We also found that the internal resistance (R_s) and the charge transfer resistance (R_{ct}) simultaneously increase. In particular, the R_{ct} sharply increases at the largest flow rates above 80 mL min^{-1}, suggesting an abrupt change in reaction kinetics attributed to the modification of the three-phase interface. Below 80 mL min^{-1}, larger flow rate may promote the penetration of the electrolyte inside the porous gas diffusion electrode (GDE) and therefore improves the reaction interface between the catalyst surface and the liquid electrolyte (**Figure 4e**). However, when further increasing the flow of electrolyte, the gas-liquid interface moves deeper inside the GDE resulting in a degraded three-phase interface and unfavorable conditions for the electrochemical reactions.[14, 33] Our experimental results highlight the critical role of interfaces for the CO_2RR in a flow cell and the optimal electrolyte flow rate corresponds to the proper balance between the surface of catalyst in contact with the electrolyte and the position of the gas-liquid interface inside the GDE. To elucidate the influence of the CO_2 feed, steady-state chronoamperometry was then recorded for different flow rates between 20 mL min^{-1} and 140 mL min^{-1} with a constant stream of electrolyte at 60 mL min^{-1}. Remarkably, the selectivity of SA Ni-NC is not influenced by the gas flow and the catalyst performs with nearly 100% selectivity towards the formation of CO over the range of potential (**Figure 4f**). The onset potential for the production of CO reaches -

0.35 V *vs.* RHE in the flow reactor – slightly more negative than that in the H-cell (**Figure** 4a and **4g**). This can be attributed to the fact that the instantaneous concentration of CO at low potentials is below the detection limit of our instrument (See Experimental section for details). At an applied potential of -0.35 V *vs.* RHE, the SA Ni-NC shows similar current densities for all flow rates; therefore indicating similar levels of CO_2RR activity (Figure 4g). At larger applied potentials, the current density increases as the CO_2 flow rates increases from 20 to 60 mL min^{-1} due to the local depletion of CO_2 near the site active at low flow rates.[32] The lower current density for the CO_2 flow rates higher than 60 mL min^{-1} points out a possible local decrease of the pH, which perturbs the CO_2 activation and the free-energy barriers in CO_2RR, in agreement with the endergonic nature of the first step. Indeed, a high feed in CO_2 will result in a large excess of CO_2 molecules not involved in the CO_2RR, which will likely induce a reduction of the local pH as previously been identified.[35,36] Overall, we identified optimal ranges for the electrolyte and CO_2 flow rates to be 40-80 mL min^{-1} and 60 mL min^{-1} respectively depending on the applied potentials **(Figure 5a**). Our results demonstrate that the potential-dependent nature of the electrocatalytic reaction rate is also controlled by the supply of CO_2 and electrolytes for the successive PCET steps.[37] Remarkably, the FE_{CO} remains $\approx$100% even at current densities larger than 100 mA cm^{-2} and the CO_2RR properties of SA Ni-NC in the flow electrolyzer are superior to those measured in the H-Cell (**Figure 5b, c**). For example, the j_{mass}, j_{total} and j_{CO} values at -0.75 V *vs.* RHE in flow electrolyzer are 2.2 A cm^{-2}, 111 mA cm^{-2} and

109.18 mA cm^{-2}, respectively. However, the values in H-cell are 0.05 A cm^{-2}, 2.31 mA cm^{-2} and 1.87 mA cm^{-2}, respectively, which are all significantly smaller than those in the flow electrolyzer. This is attributed to the *i)* better exposure of the active sites, *ii)* larger local concentration of CO_2 and *iii)* reduced amount of hydrated proton which is involved in the competitive HER.[38] To better evaluate the performance of SA Ni-NC, we calculated the evaluative parameters of the system as a function of the CO_2 flow rates at different applied potentials. The energy efficiency is found to be larger than 55 % for all the range of potentials. It reaches to 85% at -0.35 V *vs.* RHE with a current density of 7.2 mA cm^{-2} (**Figure 5d**). When considering the two important metrics, the specific current density and the energy efficiency, the SA Ni-NC catalysts in a flow reactor can achieve a current density larger than 170 mA cm^{-2} while maintaining a high energy efficiency of 56%. To gain some insight into the behavior of SA Ni-NC in the flow reactor, we also explored the role of the CO_2 feed on the yield rate of CO (**Figure 5e**). The yield rate increases with the applied potential and reached values as high as 28.4 mL min^{-1} $mg_{catalyst}^{-1}$ at an applied potential of -1.15 V *vs.* RHE and CO_2 flux of 60 mL min^{-1} – equivalent to a continuous CO production of 12.6 L min^{-1} m^{-2} of the electrode.

We further examined the single-pass CO_2-to-CO conversion, which represents the percentage of CO_2-to-CO conversion after one pass in the reactor which is the key parameter to assess the scalability of the CO_2RR system. For example, a single-pass CO_2-to-CO conversion of 10% is associated with a separation cost of 23% of the total

operation cost for the production of CO.[39] Such a value is generally considered to be a threshold target to demonstrate the industrial viability of the process. According to **Figure 5f**, it can be observed that the single-pass CO_2-to-CO conversion obeys the same trend as for j_{CO} and the largest values are obtained for electrolyte flow rates around 60 mL min^{-1}. At this specific electrolyte flow rate, the highest single-pass CO_2-to-CO conversion for the flow reactor reaches $\approx$ 3 % at a potential of -1.15 V *vs.* RHE for a CO_2 flow rate of 20 mL min^{-1} (**Figure 5g**). We also note the tendency that for a constant feed in CO_2, the single-pass CO_2-to-CO conversion values increase with the applied potential, but decreases with the CO_2 flow rate. Overall, reducing the CO_2 flow rate results in larger single-pass CO_2-to-CO conversion performance and improves the CO_2 conversion efficiency but lower the CO yield rate. Trade-offs between single-pass CO_2-to-CO conversion and CO yield rate must therefore be chosen to meet the specific industrial recommendations.

To finally demonstrate the potential of our approach, we stacked three identical flow electrolyzer using the SA Ni-NC as a CO_2RR catalyst (**Figure 6a**). The anolyte and catholyte were recycled using a peristaltic pump with a constant flow rate. The first flow electrolyzer was continuously fed with pure CO_2 and the gas outlet was successively injected in the second and third flow electrolyzer, while the downstream gas products were continuously detected *via* GC analyses. The CO_2-to-CO performances of each reactor were first examined and the specific current reached 160 $\pm$ 20 mA cm^{-2} for each electrolyzer (**Figure 6b)**. After the first two reactors, we

measured a single-pass CO_2-to-CO conversion and a CO yield rate of 4.4% and 35.3 mL min^{-1} $mg_{catalyst}^{-1}$, respectively. These values were further improved after passing through the third reactor and reached 8.9% and 71.2 mL min^{-1} $mg_{catalyst}^{-1}$ – equivalent to a continuous CO production of 31.5 L min^{-1} m^{-2}, respectively – pointing out the remarkable CO_2RR properties of SA Ni-NC in a diluted CO_2 environment **(Figure 6c**). These results allowed the identification of a quasi-linear increase of the CO_2-to-CO conversion and validated the scalability of our strategy towards higher single-pass CO_2-to-CO conversion by rationally designing the electrolyzer and the feedstock parameters. According to the linear fitting, the SA Ni-NC in a flow reactor demonstrates a single-pass conversion of 2.6% per cm^2 of the electrode for the production from CO_2-to-CO, which compares favorably to the best reports in the literature using flow electrolyzer (**Table S3**).

3. Conclusion

In summary, we have prepared single-atom nickel supported on two-dimensional nitrogen-doped carbon nanosheets using a salt template strategy. The controlled design of the single-atom Ni sites translates into high selectivity and high efficiency towards the conversion of CO_2-to-CO. When implemented in a flow electrolyzer, SA Ni-NC exhibits near-unity selectivity towards the production of CO with a specific current density as high as 170 mA cm^{-2}. Importantly, our study reveals the influence of feed-in electrolytes and CO_2 on the catalytic performance in a flow electrolyzer system. Using a model 1 cm^2 reactor, we determined the optimum flow rates for the electrolyte and

CO_2 at 40-80 mL min^{-1} and 60 mL min^{-1}, respectively – corresponding to flow speeds of 8.3-16.6 cm s^{-1} and 12.5 cm s^{-1}. The feed parameters are found to modulate the catalyst behavior in the reactor by tuning the equilibrium of the three-phase interface between the electrolyte, the CO_2 atmosphere and the surface of the electrocatalyst. This translates into a single-pass CO_2-to-CO conversion of 2.6% cm^{-2}, corresponding to a total conversion efficiency of 8.9% when stacking three 1-cm^2 reactors without a notifiable drop of the catalyst performance when operating under diluted CO_2 atmosphere. Our approach provides insight into the scalability of flow electrolyzers toward the mass production of CO from CO_2 with high Faradaic efficiency using single-atom electrocatalysts. Future developments require the further optimization of the size of the electrodes and the number of stacks for optimizing the tradeoff between the single-pass conversion and the yield rate .

4. Experimental Section

Materials:

Nickel nitrate hexahydrate ($Ni(NO_3)_2 \cdot 6H_2O$, ⩾ 98.5%), 2-methylimidazole ($CH_3C_3H_2N_2H$, 98%), methanol (CH_3OH, ⩾ 99.9%), sodium chloride (NaCl, ⩾ 99.0%), ethylene glycol ($HOCH_2CH_2OH$, 99.8%), Nickel (II) acetate tetrahydrate ($Ni(CH_3COO)_2 \cdot 4H_2O$, 98%), graphene, urea ($NH_2CONH_2$, ⩾ 99.5%), potassium sulfate (K_2SO_4, ⩾99.0%) and potassium hydroxide (KOH, 90%,) were purchased from Sigma Aldrich. Nafion (5%) and hydrochloric acid (HCl, 37%) were purchased from Alfa Aesar. All the chemicals in the experiment were used without further purification.

The gas diffusion electrode (GDE, Sigracet 29 BC) and cation exchange membrane (CEM, Nafion 117) were both purchased from the Fuel Cell Store. The fresh cathode, anode, and CEM were used for each electrolysis test to avoid contamination.

Synthesis of SA Ni-NC:

SA Ni-NC was synthesized from the graphitization of a zeolitic imidazolate metal-organic framework (ZIF). In a typical synthesis of ultrathin ZIF-67 nanosheets, 200 mg of 2-methylimidazole and 50 mg of nickel nitrate hexahydrate were dissolved in 2.5 mL of methanol, respectively.[40] After that, 20 g of the sodium chloride was mixed with the two solutions into a flask under vigorous magnetic stirring overnight at room temperature. The controlled ratio in MOF precursors and NaCl was adjusted to promote a thin coating on the salt crystals and favor the lateral growth of ZIF-67s. Subsequently, the NaCl@ZIF-67 nanosheets were obtained by the slow evaporation of the solvent at 35 ℃ followed by pyrolyzis at 800℃ for 2 hours under argon (Ar). After cooling down to room temperature, the product was soaked in 0.5 M HCl solution for 24 h at 60 ℃ to remove the redundant nickel nanoparticles. Finally, the sample was washed with deionized water for several times to remove the redundant NaCl, then centrifuged and freeze-dried for further storage.

Synthesis of Ni NPC:

The Ni nanoparticles were prepared by a modified chemical reduction method.[41] In a typical synthesis process, 0.349 g Nickel (II) acetate tetrahydrate, 17.5 mg graphene, and 1.394 g urea were mixed with 35 mL ethylene glycol through intense agitation for

0.5 h to form a homogeneous solution. Then the homogeneous solution was transferred into a 50 mL Teflon-lined stainless-steel autoclave and kept at 200 ° C for 1 h. After cooling down, the mixture was washed with ethanol for six times and dried at 80 ° C in a vacuum oven. The Ni-NPC composite was obtained by annealing the above mixture at 700 ° C in an Ar atmosphere for 10 h.

Sample characterization:

Transmission electron microscopy images (TEM) were obtained using a JEOL 1400 microscope with an emission gun operating at 120 kV. High-resolution transmission electron microscopy images (HRTEM) were obtained using JEOL 2200 FS microscope with an emission gun operating at 200 kV. The samples for electron microscopy were prepared by dropping ethanol dispersions of the samples onto 300 mesh carbon-coated copper grids and then evaporating the solvent. Aberration-corrected high-resolution scanning ttransmission electron microscopy imaging (HR-STEM), and spatially-resolved electron energy-loss spectroscopy (SR-EELS) were performed using an FEI Titan Cubed Themis microscope which was operated at 80 kV. The Themis is equipped with a double Cs aberration corrector, a monochromator, an X-FEG gun, and an ultra-high resolution energy filter (Gatan Quantum ERS) which allows for working in Dual-EELS mode. HR-STEM imaging was performed by using high-angle annular dark-field (HAADF) and annular dark-field (ADF) detectors. SR-EELS spectra were acquired with the monochromator excited allowing an energy resolution of 1.1 eV with an energy dispersion of 0.4 eV/pixel. AFM images were obtained in Digital Instruments

Nanoscope IV in tapping mode with cantilevers with a spring constant of 40 N/m and tip curvature < 10 nm and a frequency of 325 kHz (Dimension Icon, Veeco Instruments/Bruker, Germany). X-ray photoelectron spectroscopy (XPS) was performed using an ESCALAB-250 instrument (Thermo Fisher Scientific, USA), performed with a monochromatic Al-K α (1486.6 eV) radiation source and a hemisphere detector with an energy resolution of 0.1 eV. Peak positions were all corrected by the C 1s spectrum at 284.8 eV. X-ray absorption spectra (XAS) were measured at Beijing synchrotron radiation facility (BSRF) on beamline 1W1B. The storage ring is operated at a beam current of 250 mA with an electron energy of 2.5 GeV. The beam size for the sample position was $\approx 900 \times 300$ μ m^2. A Si (111) double-crystal monochromatic was applied. All of the experiments were conducted at ambient temperature and applied in the transmission mode. The curve fitting and data analysis were performed using the Artemis and IFEFFIT softwares.[42,43] The energy resolution (Δ E/E) for the incident X-ray photons was estimated to be 2×10^{-4}. Conventional transmission mode was adopted for the Ni K-edge EXAFS measurements. To verify the reproducibility of the experimental data, at least two scans were collected and analyzed for each sample.

Electrode preparation for the H-Cell reactor:

The SA Ni-NC catalyst ink was prepared by mixing 2.5 mg of SA Ni-NC powder with 9.8 mL absolute ethanol and 200 μl of Nafion solution. Subsequently, 200 μL of

the ink was drop-casted on the mechanically polished glassy carbon electrode to obtain a catalyst loading of 0.044 mg/cm² .

H-Cell assembly:

The H-Cell reactor was assembled using a Ag/AgCl reference electrode, a Pt plate counter electrode (1.5 cm x 2 cm) and a glassy carbon working electrode (1.5 cm x 1 cm). The electrolyte consisted of 0.1 M KOH and 0.5 M $K_2(SO)_4$ mixture solution, the pH value was 13.03. Before each time CO_2RR measurement, CO_2 is saturated for 30 min. The CO_2 flow is set to 5 mL min^{-1} for the long-term stability tests. All data are presented without iR-compensation.

Electrode preparation for the flow reactor:

The same amount of Ni catalyst (0.044 mg cm^{-2}) was drop-casted on the surface of GDE. The geometrical area was fixed to 1 cm^2 by the coverage of epoxy. A standard cleaning procedure was used to clean the nickel foam anode by sonication in acetone and then deionized water. The fresh cathode, anode, and CEM were used for each electrolysis test to avoid contamination. The innner diameters for the inlet and outlet tubes was 3.17 mm.

Flow electrolyzer assembly:

The model flow reactor was composed of a sandwich of flow frames, electrodes, gaskets, and a membrane as illustrated in **Figure S8** forming a three-compartment electrolyzer. One compartment delivered the CO_2 from the backside and through the GDE (2.8 x 2.8 cm^2, fixed with a PTFE frame), while the second compartment

contained the catholyte solution (0.1 M KOH + 0.5 M $K_2(SO)_4$) between the GDE and the CEM. The exposed area of the GDE was estimated to be 1 cm^2. A silver electrode was used as a quasi reference electrode. Before the experiment, the electrode was calibrated using a standard Ag/AgCl reference electrode. On the other side of the CEM, the anolyte was injected between the CEM and the nickel foam anode. The flow frames were made by PTFE, and the gaskets were made by rubber. Catholyte and anolyte were recycled using the peristaltic pump (Heidolph PD 5201).

Electrochemical measurements and gas-phase product analysis:

All of the electrochemical measurements were measured with a VSP potentiostat (Bio-Logic Science Instruments). All potentials were calibrated against the reversible hydrogen electrode (RHE) by the equation: $E_{RHE} = E_{Ag/AgCl} + 0.059\ pH + 0.197$. The products of the reaction were detected using a micro gas chromatograph (Agilent 490) and the micro-GC runs were initiated every 180 s. The GC was equipped with a packed MolSieve 5 A column and a packed HaySep D column. Argon (Praxair, 99.999%) was used as the carrier gas. A flame ionization detector with a mechanized was used to quantify CO, CH_4, and C_2H_4 while a thermal conductivity detector (TCD) was used to quantify hydrogen. The GC was calibrated by injecting a mixture calibration gas (2500 ppm CO, 2500 ppm CH_4, 2500 ppm, 2500 ppm C_2H_4, 2500 ppm C_2H_6 in CO_2, Linde). In the H-cell system, the electrolyte was first saturated with CO_2 for 30 min and gas products were detected after 30 min of reaction under potentiostat conditions. When using the flow electrolyzer, the CO_2 flow rate was tuned between 20 and 140 standard mL min^{-1} using a calibrated flow controller. The electrolyte was circulated through the anode and cathode compartments using a peristaltic pump. The gas outlet of the flow cell was directed to a condenser before being vented directly into the gas-sampling loop of the gas chromatograph. The EIS measurements were conducted at a constant potential of 0.7 V *vs.* RHE with an AC voltage of 10 mV between 100 kHz to 100 mHz

in the flow cell. The C_{dl} was calculated from linear fit of the evolution of the cathodic and anodic current density with the potential scan rates.

FIGURES

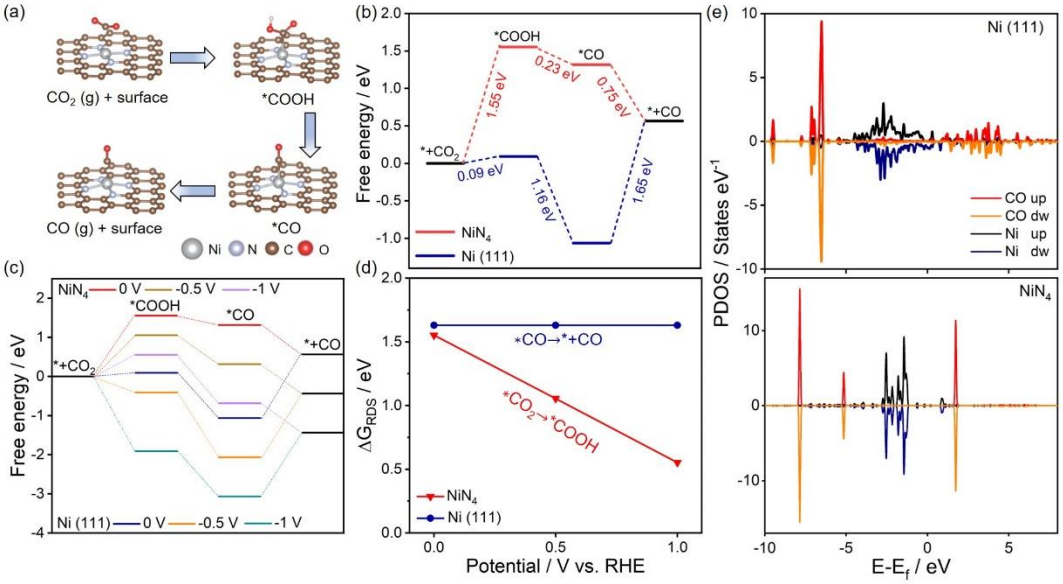

Figure 1. Theoretical and statistical predicational results on CO_2 reduction and SA Ni-NC optimizing. a, Proposed reaction pathways of SA Ni-NC for CO_2 electroreduction to CO. Silver, blue, grey and red balls represent Ni, N, C and O atoms, respectively. **b**, DFT-based free energy profile for the optimized NiN_4 and Ni (111) models during the CO_2 reduction process. **c**, Free energy diagram of the electrochemical CO_2 reduction to CO for NiN_4 and Ni (111) at increasing applied potential (V *vs.* RHE) U = 0 V, U = -0.5 V and U = -1 V. **c**, Free energy change of the limiting step (ΔG_{RDS}) at different applied potential for NiN_4 and Ni (111), respectively. **d,** Free energy diagram of hydrogen evolution for NiN_4 and Ni (111) without applied potential,

respectively. **e**, PDOS calculated by DFT for CO adsorbed on the active sites of the Ni (111) and NiN_4.

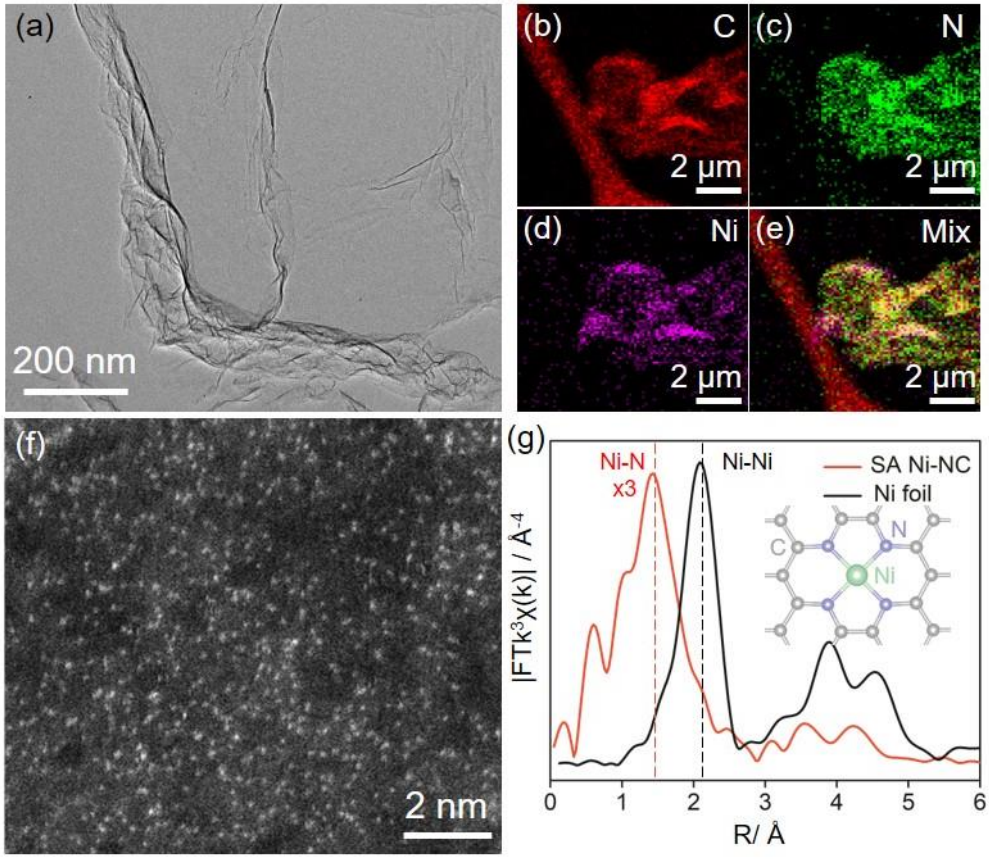

Figure 2. Characterization of the SA Ni-NC catalyst. a, Bright-field TEM image of the SA Ni-NC. b-e, The EDX mapping of the SA Ni-NC, which demonstrates the distribution of C, N, Ni. **f,** HAADF-STEM image of the SA Ni-NC. **g,** Fourier transformed EXAFS spectrum for the SA Ni-NC and Ni foil. The SA Ni-NC spectrum has been magnified 3 times.

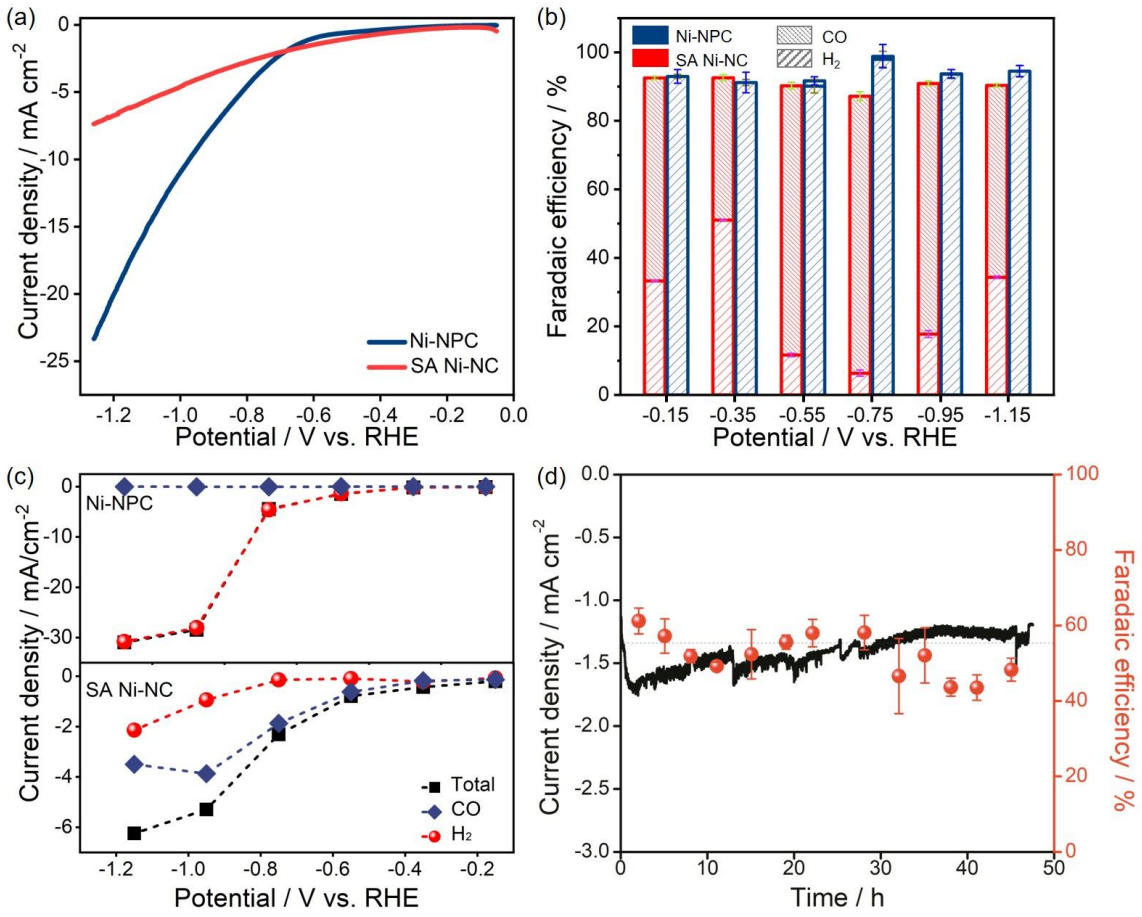

Figure 3. CO_2 electroreduction performance in the H-cell. a, LSV curves measured in CO_2-saturated 0.1 M KOH + 0.5 M K_2SO_4 mixture electrolyte of SA Ni-NC and Ni-NPC modified glassy carbon electrodes. **b,** Faradaic efficiency and **c,** partial current density at various applied potentials of the SA Ni-NC and Ni-NPC electrodes. **d,** Evolution of the cathode current density and FE_{CO} of the SA Ni-NC catalyst obtained via potentiostatic measurement at -0.8 V *vs.* RHE.

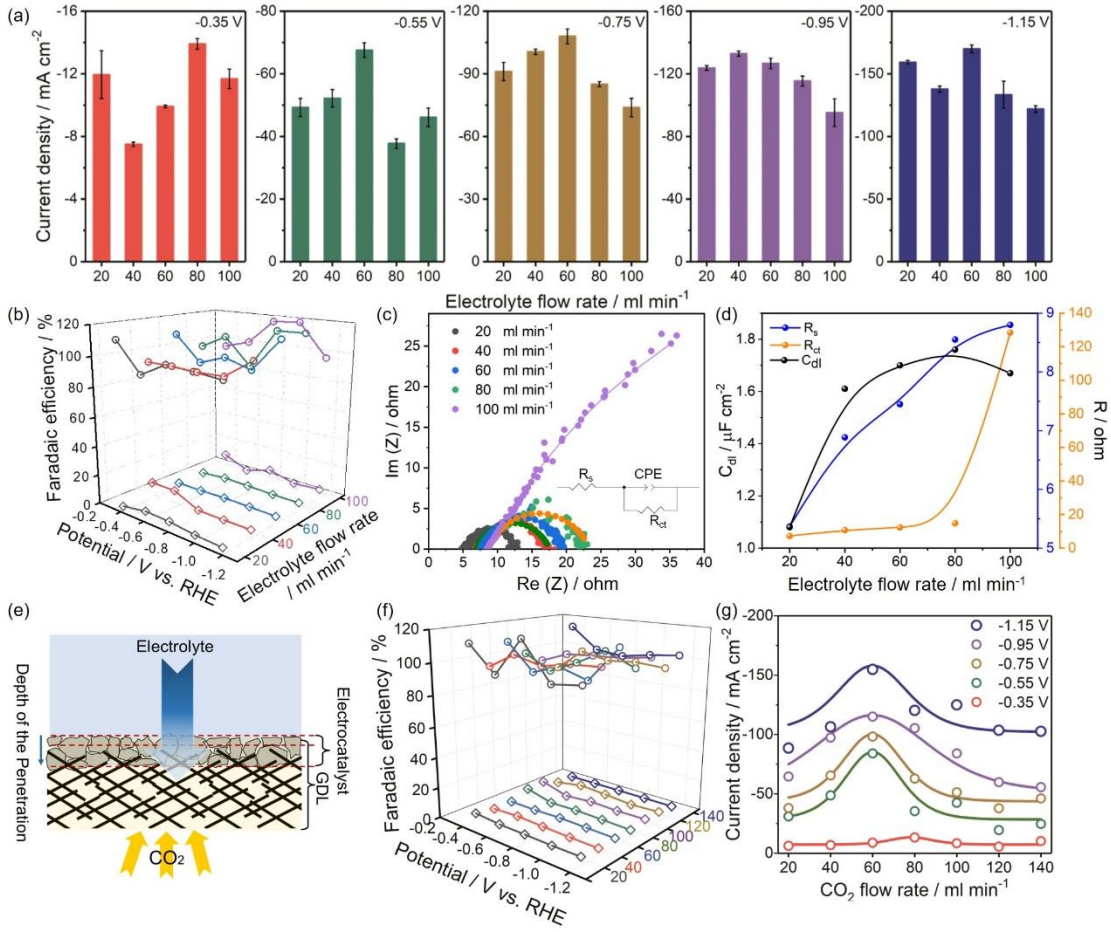

Figure 4. CO_2 electroreduction performance in the flow electrolyzer. a, Current densities for the CO_2 reduction at various applied potentials and electrolyte flow rates on SA Ni-NC catalyst. **b,** FE_{CO} measured at different applied potentials with different electrolyte flow rates. **c**, Nyquist plots of Ni SA-NC catalyst with CO_2 flow of 60 mL min^{-1} and electrolyte flow rates ranging from 20 mL min^{-1} to 100 mL min^{-1} (solid symbols are experimental results and solid lines are fitting results). **d,** C_{dl}, R_s and R_{ct} as a function of the flow rate of electrolyte for SA Ni-NC supported on the GDE in the flow cell reactor. R_s and R_{ct} are simulated based on the equivalent circuit (Insert in Figure 4c). **e,** Schematic illustration of the change of the three-phase interface with the electrolyte flow rate. **f,** FE_{CO} measured at different applied potentials with different CO_2 flow rates. **g,** Evolution of the current density with the applied potentials for different CO_2 flow rates.

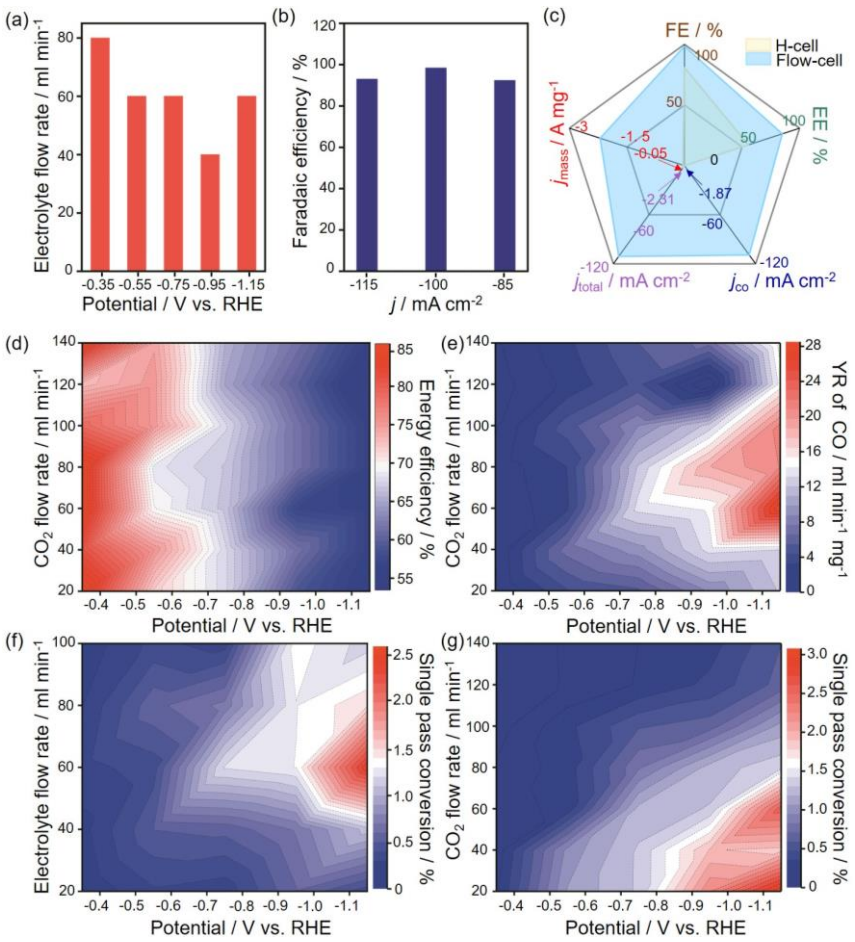

Figure 5. CO_2 electroreduction performance in the flow electrolyzer. a, Optimum electrolyte flow rates determined for each potential with a constant CO_2 flow rate. **b,** FE_{CO} values from SA Ni-NC under different current densities. **c,** CO_2RR performance from SA Ni-NC measured in the H-cell and in the flow electrolyzer (The bold values with different colors labeled in the graph are corresponding to the j_{total}, j_{mass} and j_{CO} performance in H-cell, respectively). **d and e,** 2D map of the energy efficiency (**d**) and the yield rate of CO (YR of CO) (**e**) of electrochemical CO_2 reduction from SA Ni-NC catalyst with different CO_2 flow rates with a constant electrolyte flux of 60 mL min^{-1} at different applied potentials. **f,** Single-pass CO_2 conversion for SA Ni-NC catalyst with different electrolyte flow rates at different applied potentials. **g,** Single-pass CO_2 conversion for SA Ni-NC with different CO_2 flow rates at different applied potentials.

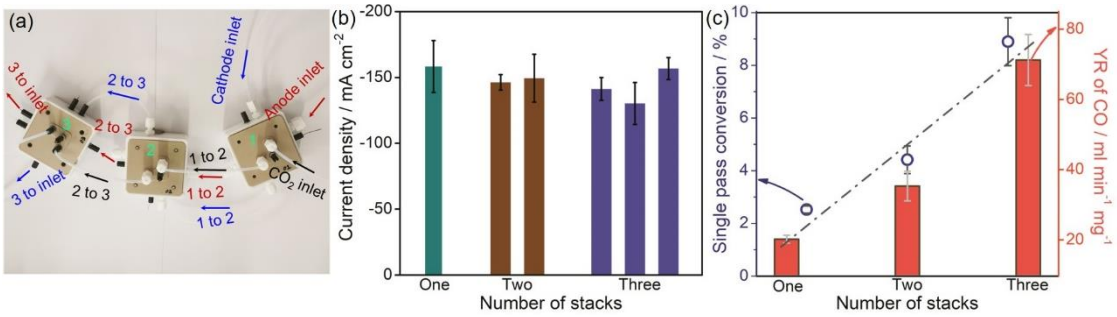

Figure 6. CO_2 electroreduction performance in the stacked flow electrolyzers. a, Scheme of the stack configuration consisting of three flow electrolyzers in series. **b,** Current densities measured by implementing with one stack, two stacks and three stacks of flow electrolyzers. **c,** Evolution of the single-pass CO_2 conversion and the yield rates for SA Ni-NC catalyst with the flow electrolyzer stack.

ASSOCIATED CONTENT

Computational details, AFM image, SEM image, HRTEM images, STEM-ADF micrographs, XPS spectra, XANES spectra, the expanded view of the flow electrolyzer and the comparison of the single-pass CO_2-to-CO conversion performance (PDF).

AUTHOR INFORMATION

Corresponding Author

*E-mail: damien.voiry@umontpellier.fr (D. Voiry).

Author Contributions

D.V., and Y. Z. designed and directed the research. Y. Z., K. Q., B. A. K., H. L. W., Y. P. Z, and W. S. W. synthesized the materials and performed the materials property

characterization. X. Q. C. and Y. W. performed the TEM, HAADF-STEM characterization and XAS experiments. F.G., E.O., and L. L. performed the HRTEM characterization. J. L. carried out and analyzed the theoretical results. Y. Z. and D. V. wrote the manuscript. D. V. supervised the project and established the final version of the paper. All authors discussed the results and commented on the manuscript. All authors have approved the final version of the manuscript.

Supporting Information. The Supporting Information is available free of charge on the ACS Publications website at DOI:

ACKNOWLEDGMENT

D.V., K.Q. and H. L. W. acknowledge funding from the European Research Council (ERC) under the European Union's Horizon 2020 research and innovation programme (grant agreement No 804320). K. Q. and Y. Z. acknowledge financial support from the China Postdoctoral Science Foundation (2018M633127) and Natural Science Foundation of Guangdong Province (2018A030310602). J. L. acknowledge financial support by the National Science Foundation of China (Grant No. 21808134). Patrice Montels and Daniel Valenza are acknowledged for their technical assistance.

REFERENCES

1 Centi, G., Quadrelli, E. & Perathoner, S. Catalysis for CO_2 conversion: a key technology for rapid introduction of renewable energy in the value chain of chemical industries. *Energy Environ. Sci.* **6**, 1711-1731 (2013).

2 Voiry, D., Shin, H., Loh, K. & Chhowalla, M. Low dimensional catalysts for hydrogen evolution and CO_2 reduction. *Nat. Rev. Chem.* **2**, 0105 (2018).

3 Qi, K., Zhang, Y., Li, J., Charmette, C., Ramonda, M., Cui, X. Q., Wang, Y., Zhang, Y. P., Wu, H. L., Wang, W. S., Zhang, X. L. & Voiry, D. Enhancing the CO_2-to-CO conversion from 2D silver nanoprisms *via* superstructure assembly. *ACS Nano* **15**, 7682-7693 (2021).

4 Creissen, C. & Fontecave, M. Solar-driven electrochemical CO_2 reduction with heterogeneous catalysts. *Adv. Energy Mater.* 2002652 (2020).

5 Gao, D., Arán-Ais, R., Jeon, H. & Cuenya, B. Rational catalyst and electrolyte design for CO_2 electroreduction towards multicarbon products. *Nat. Catal.* **2**, 198-210 (2019).

6 Chen, K. Q., Qi, K., Zhou, T., Yang, T. Q., Zhang, Y. P., Guo, Z. N., Lim, C. K., Zhang, J. Y., Žutic, I., Zhang, H. & Prasad, P. N. Water-dispersible $CsPbBr_3$ perovskite nanocrystals with ultra-stability and its application in electrochemical CO_2 reduction. *Nano-Micro Lett.* **13**, 172 (2021)

7 Qi, K., Chhowalla, M. & Voiry, D. Single atom is not alone: Metal-support interactions in single-atom catalysis. *Mater. Today* **40**, 173-192 (2020).

8 Yang, H. B., Hung, S. F., Liu, S., Yan, K., Miao, S., Zhang, L. P., Huang, X., Wang, H. Y., Cai, W. Z., Chen, R., Gao, J. J., Yang, X. F., Chen, W., Huang, Y. Q., Chen, H. M., Li, C. M., Zhang, T. & Liu, B. Atomically dispersed Ni(i) as the active site for electrochemical CO_2 reduction. *Nat. Energy* **3**, 140-147 (2018).

9 Zheng, T. T., Jiang, K., Ta, N., Hu, Y. F., Zeng, J., Liu, J. Y., & Wang, H. T. Large-scale and highly eelective CO_2 electrocatalytic reduction on nickel single-atom catalyst. *Joule* **3**, 265-278 (2019).

10 Gong, L. L., Zhang, D. T., Lin, C. Y., Zhu, Y. H., Shen, Y., Zhang, J., Han, X., Zhang, L. P. & Xia, Z. H. Catalytic mechanisms and design principles for

single-atom catalysts in highly efficient CO_2 conversion. *Adv. Energy Mater*. **9**, 1902625 (2019).

11 Wang, Y., Qi, K., Yu, S. S., Jia, G. R., Cheng, Z. L., Zheng, L. R., Wu, Q., Bao, Q. L., Wang, Q. Q., Zhao, J. X., Cui, X. Q. & Zheng, W. T. Revealing the intrinsic peroxidase-like catalytic mechanism of heterogeneous single-atom Co-MoS_2. *Nano-Micro Lett.* **11**, 1-13 (2019).

12 Qi, K., Cui, X. Q., Gu, L., Yu, S. S., Fan, X. F., Luo, M. C., Xu, S., Li, N. B., Zheng, L. R., Zhang, Q. H., Ma, J. Y., Gong, Y., Lv, F., Wang, K., Huang, H. H., Zhang, W., Guo, S. J., Zheng, W. T. & Liu, P. Single-atom cobalt array bound to distorted 1T MoS_2 with ensemble effect for hydrogen evolution catalysis. *Nat. Commun.* **10**, 5231 (2019).

13 Choi, H., Lee, D. K., Han, M. K., Janani, G., Surendran, S., Kim, J. H., Kim, J. K., Cho, H. & Sim, U. Review—Non-noble metal-based single-atom catalysts for efficient electrochemical CO_2 reduction reaction. *J. Electrochem. Soc.* **167**, 164503 (2020).

14 García de Arquer, F., Dinh, C. T., Ozden, A., Wicks, J., Mccallum, C., Kirmani, A. R., Nam, D. H., Gabardo, C., Seifitokaldani, A., Wang, X., Li, Y. C., Li, F. W., Edwards, J., Richter, L. J., Thorpe, S. J., Sinton, D. & Sargent, E. H CO_2 electrolysis to multicarbon products at activities greater than 1 A cm^{-2}. *Science* **367**, 661 (2020).

15 Ren, S. X., Joulié, D., Salvatore, D., Torbensen, K., Wang, M., Robert, M., & Berlinguette, C. P. Molecular electrocatalysts can mediate fast, selective CO_2 reduction in a flow cell. *Science* **365**, 367-369 (2019).

16 Yang, H. P., Lin, Q., Zhang, C., Yu, X. Y., Cheng, Z. Li, G. D., Hu, Q., Ren, X. Z., Zhang, Q. L., Liu, J. H. & He, C. X. Carbon dioxide electroreduction on single-atom nickel decorated carbon membranes with industry compatible current densities. *Nat. Commun.* **11**, 593 (2020).

17 Salvatore, D. & Berlinguette, C. Voltage matters when reducing CO_2 in an electrochemical flow cell. *ACS Energy Lett.* **5**, 215-220 (2019).

18 Gabardo, C. M., Seifitokaldani, A., Edwards, J. P., Dinh, C. T., Burdyny, T., Kibria, M. G., O'Brien, C. P., Sargent, E. H. & Sinton, D. Combined high alkalinity and pressurization enable efficient CO_2 electroreduction to CO. *Energy Environ. Sci.* **11**, 2531-2539 (2018).

19 Ma, M. Chark, E. L., Therkildsen, K. T., Dalsgaard, S., Chorkendorff, Ib. & Seger, B. *et al.* Insights into the carbon balance for CO_2 electroreduction on Cu using gas diffusion electrode reactor designs. *Energy Environ. Sci.* **13**, 977-985 (2020).

20 Millet, M. M., Siller, G. A., Wrabetz, S., Mazheika, A., Girgsdies, F., Teschner, D., Seitz, F., Tarasov, A., Levchenko, S. V., Schlögl, R. & Frei, E. Ni single atom catalysts for CO_2 activation. *J. Am. Chem. Soc.* **141**, 2451-2461 (2019).

21 Kim, B., Hillman, F., Ariyoshi, M., Fujikawa, S. & Kenis, P. Effects of composition of the micro porous layer and the substrate on performance in the electrochemical reduction of CO_2 to CO. *J. Power Sources* **312**, 192-198 (2016).

22 Gabardo, C. M., O'Brien, C. P., Edwards, J. P., McCallum, C., Xu, Y., Dinh, C. T., Li, J., Sargent, E. H. & Sinton, D. Continuous carbon cioxide electroreduction to concentrated multi-carbon products using a membrane electrode assembly. *Joule* **3**, 2777-2791 (2019).

23 Tan, Y., Lee, K., Song, H. & Oh, J. Modulating Local CO_2 concentration as a general strategy for enhancing C-C coupling in CO_2 electroreduction. *Joule* **4**, 1104-1120 (2020).

24 Song, H., Im, M., Song, J. T., Lim, J. A., Kim, B. S., Kwon, Y., Ryu, S. & Oh, J. *et al.* Effect of mass transfer and kinetics in ordered Cu-mesostructures for electrochemical CO_2 reduction. *Appl. Catal. B* **232**, 391-396 (2018).

25 Lum, Y. & Ager, J. Sequential catalysis controls selectivity in electrochemical CO_2 reduction on Cu. *Energy Environ. Sci.* **11**, 2935-2944 (2018).

26 Endrődi, B., Kecsenovity, E., Samu, A., Darvas, F., Jones, R. V., Török, V., Danyi, A. & Janáky. C. Multilayer electrolyzer stack converts carbon dioxide to gas products at high pressure with high efficiency. *ACS Energy Lett.* **4**, 1770-1777 (2019).

27 Yang, H. P., Wu, Y., Lin, Q., Fan, L. D., Chai, X. Y., Zhang, Q. L., Liu, J. H., He, C. X. & Lin. Z. Q. Composition tailoring via N and S co-doping and structure tuning by constructing hierarchical pores: Metal-free catalysts for high-performance electrochemical reduction of CO_2. *Angew. Chem. Int. Ed.* **130**, 15702-15706 (2018).

28 Möller, T., Ju, W., Bagger, A., Wang, X. L., Luo, F., Thanh, T. N., Varela, A. S., Rossmeisl, J. & Strasser, P. Efficient CO_2 to CO electrolysis on solid Ni-N-C catalysts at industrial current densities. *Energy Environ. Sci.* **12**, 640-647 (2019).

29 Nesbitt, H., Legrand, D. & Bancroft, G. M. Interpretation of Ni2p XPS spectra of Ni conductors and Ni insulators. *Phys Chem Miner.* **27**, 357-366 (2000).

30 Zhang, T., Lin, L. L., Li, Z. Y., He, X. Y., Xiao, S. D., Shanov, V. N. & Wu, J. J. Nickel-nitrogen-carbon molecular catalysts for high rate CO_2 electro-reduction to CO: On the role of carbon substrate and reaction chemistry. *ACS Appl. Energy Mater.* **3**, 1617-1626 (2020).

31 García de Arquer, F., Bushuyev, O. S., Luna, P. D., Dinh, C. T., Seifitokaldani, A., Saidaminov, M. I., Tan, C. S., Quan, L. N., Proppe, A., Kibria, M. G., Kelley, S. O., Sinton, D. & D. Sargent, E. H. 2D metal oxyhalide-derived catalysts for efficient CO_2 electroreduction. *Adv. Mater.* **30**, 1802858 (2018).

32 Jouny, M., Luc, W. & Jiao, F. High-rate electroreduction of carbon monoxide to multi-carbon products. *Nat. Catal.* **1**, 748-755 (2018).

33 Bienen, F., Kopljar, D., Löwe, A., Geiger, S., Wagner, N., Klemm, E. & Friedrich, K. A. Revealing mechanistic processes in gas-diffusion electrodes during CO_2 reduction *via* impedance spectroscopy. *ACS Sustainable Chem. Eng.* **8**, 13759–13768 (2020).

34 Bondue, C., Graf, M., Goyal, A. & Koper, M. Suppression of hydrogen evolution in acidic electrolytes by electrochemical CO_2 reduction. *J. Am. Chem. Soc.* **143**, 279-285 (2020).

35 Li, J., Chen, G. X., Zhu, Y. Y., Liang, Z., Pei, A. Wu, C. L., Wang, H. X., Lee, H. R., Liu, K., Chu, S. & Cui, Y. Efficient electrocatalytic CO_2 reduction on a three-phase interface. *Nat. Catal.* **1**, 592-600 (2018).

36 Singh, M., Goodpaster, J., Weber, A., Head-Gordon, M. & Bell, A. Mechanistic insights into electrochemical reduction of CO_2 over Ag using density functional theory and transport models. *Proc. Natl. Acad. Sci. U.S.A* **114**, E8812-E8821 (2017).

37 Shinagawa, T., Garcia-Esparza, A. & Takanabe, K. Insight on Tafel slopes from a microkinetic analysis of aqueous electrocatalysis for energy conversion. *Sci. Rep.* **5**, 13801 (2015).

38 Nguyen, D., Lee, W. C., Na, J., Kim, M. C., Kha Tu, N. D., Lee, S. Y., Sa, Y. J., Won, D. H., Oh, H. S., Kim, H., Min, B. K., Han, S. S., Lee, U. & Hwang, Y. J. Mass transport control by surface graphene oxide for selective CO production from electrochemical CO_2 reduction. *ACS Catal.* **10**, 3222-3231 (2020).

39 Jeng, E. & Jiao, F. Investigation of CO_2 single-pass conversion in a flow electrolyzer. *React. Chem. Eng.* **5**, 1768-1775 (2020).

40 Huang, L., Zhang, X. P., Han, Y. J., Wang, Q. Q., Fang, Y. X. & Dong, S. J. In situ synthesis of ultrathin metal0organic framework nanosheets: A new method for 2D metal-based nanoporous carbon electrocatalysts. *J. Mater. Chem. A* **5**, 18610-18617 (2017).

41 Zhang, Z., Wang, X. G., Zhang, X., Xie, Z. J., Chen, Y. N., Ma, L. P., Peng, Z. Q. & Zhou, P. Z. Verifying the rechargeability of Li-CO_2 batteries on working cathodes of Ni nanoparticles highly dispersed on N-doped graphene. *Adv. Sci.* **5**, 1700567 (2018).

42 Rehr, J. & Albers, R. Theoretical approaches to X-ray absorption fine structure. *Rev. Mod. Phys.* **72**, 621 (2000).

43 Newville, M. EXAFS analysis using FEFF and FEFFIT. *J. Synchrotron. Radiat.* **8**, 96-100 (2001).